Measurement 222 (2023) 113690

Contents lists available at ScienceDirect

Measurement

journal homepage: www.elsevier.com/locate/measurement

Augmenting inertial motion capture with SLAM using EKF and SRUKF data fusion algorithms

Mohammad Mahdi Azarbeik *, Hamidreza Razavi, Kaveh Merat, Hassan Salarieh

Department of Mechanical Engineering, Sharif University of Technology, Azadi Ave, Tehran, Iran

ARTICLE INFO

Dataset link: https://ieee-dataport.org/documents/human-arm-motion-tracking-fusion-imu-modules-and-slam-method-compared-vicon

Keywords:
Sensor fusion
Motion capture
Inertial sensors
Extended and unscented Kalman filter
SLAM

ABSTRACT

This paper proposes quaternion-based extended and square-root unscented Kalman filters to estimate human body segment positions and orientations using low-cost IMUs in conjunction with a SLAM method. The Kalman filters use measurements based on SLAM output, multilink biomechanical constraints, and vertical referencing to correct errors. In addition to the sensor biases, the fusion algorithm is capable of estimating link geometries, allowing the imposition of biomechanical constraints without *a priori* knowledge of sensor positions. The proposed algorithms achieve up to 5.87 (cm) and 1.1 (deg) accuracy in position and attitude estimation in various scenarios of human arm movements. Compared to the EKF, the SRUKF algorithm presents a smoother and higher convergence rate but is 2.4 times more computationally demanding. After convergence, the SRUKF is up to 17% less and 36% more accurate than the EKF in position and attitude estimation, respectively.

1. Introduction

Several techniques have been developed to monitor human body movements. These techniques have many applications in biomedical science (e.g. for monitoring patients' progress during rehabilitation), virtual and augmented reality, human-machine interaction, and the movie industry. Recently, inertial motion capture using inertial measurement units (IMUs) has drawn more attention than traditional marker-based optical techniques due to its low cost, small sensor size, and ability to be used in non-laboratory environments [1]. The main disadvantage of accurate optical motion tracking systems is that they are mostly practical in laboratory and indoor environments. Additionally, visual sensors suffer from occlusion when targets are obstructed by other joints, limbs, or objects [2]. Another motion capture method relies on Microsoft Kinect [3] which besides occlusion, suffers from a low sampling rate [4]. Also, when a single Kinect sensor is used to track human movements, the subject must always face Kinect, because the tracking errors will increase significantly when the target rotates. Consequently, several Kinect sensors should be used and their data should be merged [5,6].

An IMU consists of an orthogonal tri-axis gyroscope, an orthogonal tri-axis accelerometer, and an orthogonal tri-axis magnetometer sensor. Rigid body orientation can be achieved using an IMU which facilitates tracking of human segment movements by attaching the IMU to the body segments [7], therefore, the orientations of the body links can be estimated by means of the IMU data attached to the body links [8]. However, uncalibrated sensor [9] and drift [10] problems affect IMUs data, especially in dynamic motions. Calibration methods for accelerometer, magnetometer, and gyroscope, are introduced in [11]. Furthermore, human body localization is not feasible through IMU data alone due to the presence of stochastic disturbances (measurement noise) and systematic disturbances (e.g. bias) on IMU outputs that manifest as drift once integrated. Several studies have been performed to determine the orientation of the IMU sensors. In [12,13], low computational cost complementary filters for increased accuracy in estimating attitude are proposed. Attitude and joint angles estimation between two consecutive segments of the human body, using only accelerometers and gyroscopes via a Markov approach is proposed in [14]. In [15], a method for estimating arm attitude based on an IMU and Kinect sensor measurements via an unscented Kalman filter data fusion algorithm is introduced. Given the limited visual range of the Kinect sensor, the authors evaluated the accuracy of the proposed algorithm without Kinect support in [16]. Inertial motion capture algorithms capable of estimating sensor parameters and link geometry in real-time based on extended and unscented Kalman filtering were introduced and compared in [17].

Intensive research on simultaneous localization and mapping (SLAM) and visual odometry (VO) systems using cameras alone, or combined with inertial sensors, have produced methods to estimate the position and orientation of a particular target [18]. SLAM methods construct or update a map of an unknown environment while

* Corresponding author.
E-mail address: mm.azarbeik@gmail.com (M.M. Azarbeik).

https://doi.org/10.1016/j.measurement.2023.113690
Received 16 May 2023; Received in revised form 29 September 2023; Accepted 8 October 2023
Available online 16 October 2023

simultaneously tracking the position of an agent. A system capable of performing visual, visual-inertial, and multi-map SLAM with one or two camera(s) and different lens models, "ORB-SLAM3", is proposed in [18]. In [19], the semidirect VO "SVO", which is significantly faster than many of the state-of-the-art VO algorithms, is proposed. Although SVO is competitively accurate, its accuracy is still significantly lower than ORB-SLAM3. In [20], IMU is used to overcome localization in case of insufficient light and texture. Moreover, a multi-state constrained Kalman filter algorithm is used for visual and inertial data fusion to improve the accuracy and efficiency of the visual-inertial odometry system positioning. As stated, IMUs data alone is insufficient for body links' position estimation. Therefore, this research uses a SLAM method (ORB-SLAM3 [18]) alongside these sensors to estimate the position of the links.

The fusion algorithms proposed in this study augment the method in [17] by introducing body-mounted camera data into the system. This work presents an inertial motion capture algorithm combined with a SLAM method (ORB-SLAM3 [18]) as reference position measurement, based on extended and square-root unscented Kalman filtering, capable of estimating the positions and attitudes of multiple body links in unknown, outdoor, and non-laboratory environments, with appropriate accuracy. Due to the well-defined error models to minimize the effects of measurement noise on the corresponding error dynamics, simple sensor fusion algorithms such as EKF are able to handle the system nonlinearities. However, the performance of the Kalman filter in parameter estimation correction is evaluated using extended and unscented Kalman filters to assess different Kalman filtering schemes on estimation accuracy and convergence rate. As the conventional unscented Kalman filter suffers from numerical instability issues, a square-root covariance propagation and update algorithm is used to mitigate this issue. The computational cost of the unscented Kalman filter increases substantially as the number of the estimated states increases. Gyroscopes and accelerometers biases, which for low-cost IMUs tend to change with temperature and passage of time, are estimated alongside the position, velocity, attitude, and geometry of body links. Although IMUs consist of accelerometers, gyroscopes, and magnetometers, in this study, the magnetometers data were disregarded due to the existence of magnetic disturbances in the laboratory environment. The position and velocity of each joint are obtainable using the data from the two adjacent modules, which ideally, should be equivalent. However, due to joint deformations, these positions and velocities will not be exactly equal. Measurements based on these biomechanical constraints present in a multi-link system, SLAM output using the camera, and vertical referencing using accelerometer data are used for error control in the correction step of the Kalman filters. The ability to estimate body links geometry allows the imposition of biomechanical constraints without *a priori* knowledge of the sensors and the camera positioning [21]. Additionally, stationary accelerometer data are used as a complementary measurement to the filter for attitude estimation correction. Combining multi-link inertial motion capture with the SLAM method for human body localization and pose estimation making the motion capture system practical in any environment is the main innovation of the present study. The VICON optical motion capture system is used as a verification ground-truth to evaluate the performance of the proposed algorithms. Moreover, since ORB-SLAM3 itself includes errors and suffers from low and disordered output frequency, shoulder reference position measurements are fed to the data fusion algorithms once using the SLAM method and once using the VICON optical motion capture system to evaluate the performance of the algorithms, disregarding the errors of the SLAM system.

2. Fundamentals

This section describes the system overview, various reference frames, dynamic equations, and sensor output models used throughout the paper which are based on [17].

Table 1
Nomenclature.

Symbol	Description
J_{ij}	The joint between the ith and jth links
$l_{ij}^{b_i}$	The vector connecting the ith module to J_{ij}
$l_c^{b_0}$	Lever arm connecting the 0th module to the camera
n	NED (North-East-Down) frame
b_k	kth module sensor body frame
p_k	kth module's estimation of the n-frame
$(.)_c$	Variable is associated with the camera
$\bar{(.)}$	Measured value
$\hat{(.)}$	Estimated value

The multi-body system the motion of which is to be captured consists of N links, each being connected to at least one other link via a ball and socket joint. The vectors connecting the sensor modules of ith and jth links to their connecting joint, J_{ij}, will be denoted by segment $l_{ij}^{b_i} \in \mathbb{R}^3$ and $l_{ji}^{b_j} \in \mathbb{R}^3$ (Fig. 1) [17]. The camera is assumed to be installed on the 0th module and the lever arm connecting the 0th module to the camera is denoted by $l_c^{b_0} \in \mathbb{R}^3$. The recurring symbols used throughout the paper are tabulated in Table 1.

In this article, the direction cosine matrix (DCM), quaternion, and rotation vector described in [22] are used to parameterize rotations. The symbol $\otimes$ refers to the quaternion product defined as,

$$\mathbf{q}_1 \otimes \mathbf{q}_2 = \begin{bmatrix} q_1 q_2 - \mathbf{q}_{1v} \cdot \mathbf{q}_{2v} \\ q_1 \mathbf{q}_{2v} + q_2 \mathbf{q}_{1v} + \mathbf{q}_{1v} \times \mathbf{q}_{2v} \end{bmatrix} \tag{1}$$

$$\mathbf{q}^T = \begin{bmatrix} q & \mathbf{q}_v^T \end{bmatrix} \tag{2}$$

where q_1, q_2, q and $\mathbf{q}_{1v}, \mathbf{q}_{2v}, \mathbf{q}_v \in \mathbb{R}^3$ represent the scalar and vector parts of unit quaternions $\mathbf{q}_1$, $\mathbf{q}_2$, and $\mathbf{q}$, respectively.

For an arbitrary vector $\mathbf{z}$ the symbols $\hat{\mathbf{z}}$ and $\tilde{\mathbf{z}}$ indicate the estimated and measured values of $\mathbf{z}$, respectively, and $\delta\mathbf{z}$ denotes the estimation error vector.

$$\mathbf{z} = \delta\mathbf{z} + \hat{\mathbf{z}} \tag{3}$$

The quaternion form of vector $\mathbf{d} \in \mathbb{R}^3$ is represented by,

$$\bar{\mathbf{d}}^T = \begin{bmatrix} 0 & \mathbf{d}^T \end{bmatrix} \tag{4}$$

The n-frame denotes the NED (North-east-down) frame, the b_k-frame refers to the kth module sensor body frame, and the p_k-frame is the kth module's estimation of the n-frame which satisfies [22],

$$\hat{\mathbf{R}}_{b_k}^n = \mathbf{R}_{b_k}^{p_k} \tag{5a}$$

$$\hat{\mathbf{q}}_{b_k}^n = \mathbf{q}_{b_k}^{p_k} \tag{5b}$$

where $\hat{\mathbf{q}}_{b_k}^n$ and $\mathbf{q}_{b_k}^{p_k}$ are the quaternion equivalents of DCMs $\hat{\mathbf{R}}_{b_k}^n$ and $\mathbf{R}_{b_k}^{p_k}$, respectively.

In this study, the effects of the earth's rotational velocity will be neglected due to the relatively larger measurement noise and resolution. Consequently, the dynamic model equations of the kth module are obtained by simplifying the equations of the inertial navigation system [22],

$$\dot{\mathbf{p}}_k^n = \mathbf{v}_k^n \tag{6a}$$

$$\dot{\mathbf{v}}_k^n = \mathbf{R}_{b_k}^n \mathbf{f}_k^{b_k} + \mathbf{g}^n \tag{6b}$$

$$\dot{\mathbf{q}}_{b_k}^n = \frac{1}{2} \mathbf{q}_{b_k}^n \otimes \bar{\boldsymbol{\omega}}_{ib_k}^{b_k} \tag{6c}$$

where the vectors $\mathbf{p}_k^n, \mathbf{v}_k^n \in \mathbb{R}^3$ denote the position and velocity of the kth module in the n-frame, respectively. The gravity vector in the n-frame is denoted as $\mathbf{g}^n \in \mathbb{R}^3$. The vectors $\mathbf{f}_k^{b_k}, \boldsymbol{\omega}_{ib_k}^{b_k} \in \mathbb{R}^3$ refer to the specific force and rotational velocity of the kth module expressed in the b_k-frame, respectively. The unit quaternion $\mathbf{q}_{b_k}^n \in \mathbb{R}^4$ and rotation

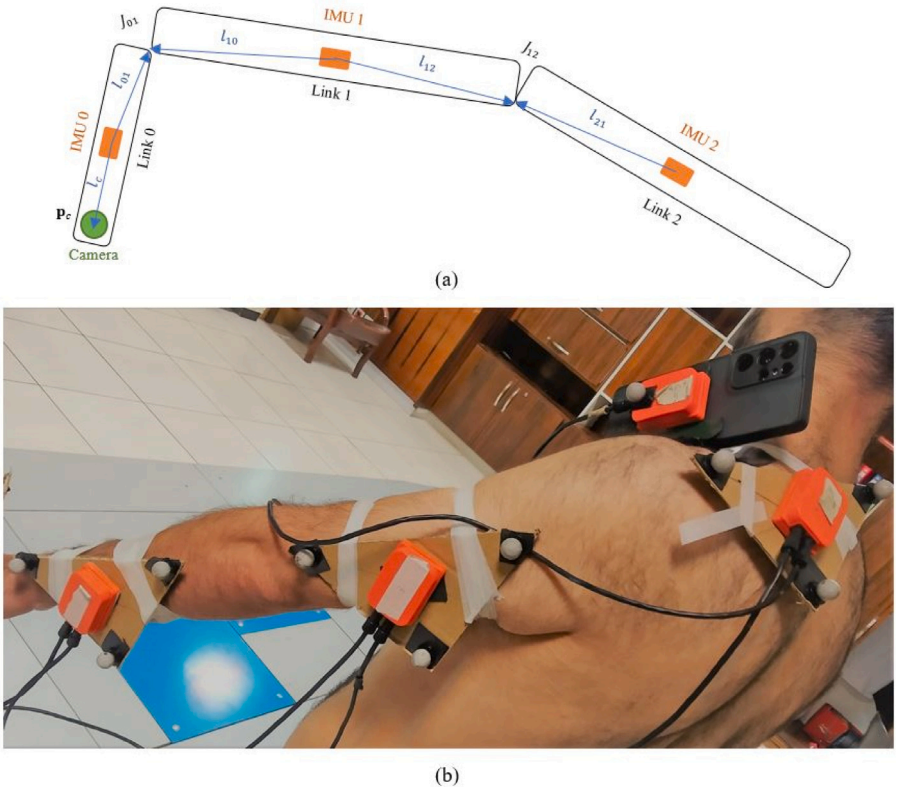

Fig. 1. (a) Schematic of sensors, links, and markers placement. (b) Experimental setup. (The data of the IMU attached to the camera is only used for the ORB-SLAM3.)

matrix $\mathbf{R}^{n}_{b_k} \in \mathbb{R}^{3\times3}$ parameterize the b_k-frame attitude in relation to the n-frame.

Due to sensor bias, scaling, non-orthogonality, and measurement noise, the accelerometer and gyroscope outputs differ from the actual values of specific force and angular velocity. As shown in [17], the estimation accuracy in inertial motion capture scenarios is not necessarily enhanced by adaptive estimation of accelerometer and gyroscope scaling and non-orthogonality parameters due to their poor observability. Therefore, the IMUs outputs are modeled by,

$$\mathbf{f}^{b_k}_{k} = \tilde{\mathbf{f}}^{b_k}_{k} - \mathbf{b}_{a,k} - \boldsymbol{\eta}_{a,k} \tag{7a}$$

$$\boldsymbol{\omega}^{b_k}_{ib_k} = \tilde{\omega}^{b_k}_{ib_k} - \mathbf{b}_{g,k} - \boldsymbol{\eta}_{g,k} \tag{7b}$$

where the indexes $(.)_{a,k}$ and $(.)_{g,k}$ correspond respectively to the accelerometer and the gyroscope of the kth module. The vectors $\mathbf{b} \in \mathbb{R}^3$ and $\boldsymbol{\eta} \in \mathbb{R}^3$ represent the bias and white Gaussian measurement noise vectors, respectively. The diagonal covariance matrices of $\boldsymbol{\eta}_{a,k}$ and $\boldsymbol{\eta}_{g,k}$ are $\sigma_{a,k}\mathbf{I}_{3\times3}$ and $\sigma_{g,k}\mathbf{I}_{3\times3}$, respectively, where $\sigma_{a,k} > 0$ and $\sigma_{g,k} > 0$ represent the axiswise noise standard deviations (SD). According to (7),

$$\hat{\mathbf{f}}^{b_k}_{k} \approx \tilde{\mathbf{f}}^{b_k}_{k} - \hat{\mathbf{b}}_{a,k} \tag{8a}$$

$$\hat{\boldsymbol{\omega}}^{b_k}_{ib_k} \approx \tilde{\boldsymbol{\omega}}^{b_k}_{ib_k} - \hat{\mathbf{b}}_{g,k} \tag{8b}$$

3. Error models

Considering (3), (7), and (8) the sensor output errors are modeled as,

$$\delta\mathbf{f}^{b_k}_{k} = \mathbf{f}^{b_k}_{k} - \hat{\mathbf{f}}^{b_k}_{k} = -\delta\mathbf{b}_{a,k} - \boldsymbol{\eta}_{a,k} \tag{9a}$$

$$\delta\boldsymbol{\omega}^{b_k}_{ib_k} = \boldsymbol{\omega}^{b_k}_{ib_k} - \hat{\boldsymbol{\omega}}^{b_k}_{ib_k} = -\delta\mathbf{b}_{g,k} - \boldsymbol{\eta}_{g,k} \tag{9b}$$

The attitude quaternion estimation error, unlike the other system parameters which follow (3), is modeled as,

$$\mathbf{q}^{n}_{b_k} = \mathbf{q}^{n}_{p_k} \otimes \mathbf{q}^{p_k}_{b_k} \tag{10}$$

where $\mathbf{q}^{n}_{p_k}$ represents the n-frame attitude estimation error and is used to rotate its axes to obtain the p_k-frame axes. The rotation vector equivalent of $\mathbf{q}^{n}_{p_k}$ is indicated by $\boldsymbol{\phi}_k$.

The present inertial motion capture algorithm is implemented using both extended and unscented Kalman filters. Since the unscented implementation calculates sigma points, it only requires the parameter estimation error models, system dynamics, and measurement equations. However, the extended implementation requires the estimation error dynamics and error-based measurement residuals [23]. To obtain the estimation error dynamics required for the extended Kalman filter, $\boldsymbol{\phi}_k$ is assumed to be small (i.e. $\|\boldsymbol{\phi}_k\| \ll 1$). Therefore, $\mathbf{R}^{n}_{p_k}$, the DCM representing the rotation between the n-frame and p_k-frame, and its quaternion equivalent, $\mathbf{q}^{n}_{p_k}$, satisfy these equations [22]:

$$\mathbf{R}^{n}_{p_k} \approx \mathbf{I}_{3\times3} + [\boldsymbol{\phi}_k\times] \tag{11a}$$

$$(\mathbf{q}^{n}_{p_k})^T \approx [1 \quad \tfrac{1}{2}\boldsymbol{\phi}_k{}^T] \tag{11b}$$

Subsequently, differentiating (10) with respect to time, while considering (6c) and (11b), we have

$$\dot{\mathbf{q}}^{n}_{p_k} = \frac{1}{2}\mathbf{q}^{n}_{p_k} \otimes \delta\bar{\boldsymbol{\omega}}^{p_k}_{ib_k} \tag{12}$$

Considering (9b), (11b), (12), small angle rotation vector dynamics, and omitting higher order terms results in [22],

$$\dot{\boldsymbol{\phi}}_k \approx \delta\boldsymbol{\omega}^{p_k}_{ib_k} \tag{13}$$

Taking into account (3), differentiating the velocity estimation with respect to time and substituting by (6b), (7a), (9a), and (11a) leads to,

$$\delta\dot{\mathbf{v}}^{n}_{k} = \delta\mathbf{f}^{p_k}_{k} - \hat{\mathbf{f}}^{p_k}_{k} \times \boldsymbol{\phi}_k \tag{14}$$

Taking into account (3), differentiating the position estimation error with respect to time and substitution of (6a) results in:

$$\delta\dot{\mathbf{p}}_k^n = \delta\mathbf{v}_k^n \tag{15}$$

4. Sensor fusion

As a result of measurement noise, incorrect parameter initialization, and numerical integration, position, velocity, and attitude estimation of each link using the differential equations of (6) are subject to error. In both extended and unscented Kalman filters, measurements based on biomechanical constraints present in a multi-link body system, reference position measurement using SLAM output via the camera or the VICON optical motion capture system, and vertical referencing using accelerometer measurements are used to correct these errors. The position and velocity of each joint are obtainable using the position, velocity, and attitude of the adjacent link module. Considering (Fig. 1),

$$\mathbf{p}_{J_{ij},i}^n = \mathbf{p}_i^n + \mathbf{R}_{b_i}^n \mathbf{l}_{ij}^{b_i} \tag{16}$$

where $\mathbf{p}_{J_{ij},i}^n$ is the position of the joint J_{ij} obtained from the ith link parameters. Ideally, $\mathbf{p}_{J_{ij},i}^n$ and $\mathbf{p}_{J_{ij},j}^n$ should be equivalent, however, the body joints deform slightly during motions. For the purpose of imposing the equivalence constraint between $\mathbf{p}_{J_{ij},i}^n$ and $\mathbf{p}_{J_{ij},j}^n$, the following pseudo-measurement vector is defined considering (16) to model the joints' deformations,

$$\tilde{\mathbf{y}}_{p_{ij}} = \mathbf{p}_j^n - \mathbf{p}_i^n + \mathbf{R}_{b_j}^n \mathbf{l}_{ji}^{b_j} - \mathbf{R}_{b_i}^n \mathbf{l}_{ij}^{b_i} + \boldsymbol{\eta}_{p,J_{ij}} \tag{17}$$

where the diagonal covariance matrix of $\boldsymbol{\eta}_{p,J_{ij}} \in \mathbb{R}^3$ is $\sigma_{p,J_{ij}}\mathbf{I}_{3\times3}$ with $\sigma_{p,J_{ij}} > 0$ representing the axiswise noise SD. Considering (17) and (5a),

$$\hat{\mathbf{y}}_{p_{ij}} = \hat{\mathbf{p}}_j^n - \hat{\mathbf{p}}_i^n + \mathbf{R}_{b_j}^{p_j} \hat{\mathbf{l}}_{ji}^{b_j} - \mathbf{R}_{b_i}^{p_i} \hat{\mathbf{l}}_{ij}^{b_i} \tag{18}$$

The joint's position residual vector, $\delta\mathbf{y}_{P_{ij}} \in \mathbb{R}^3$, is defined as,

$$\delta\mathbf{y}_{P_{ij}} = \tilde{\mathbf{y}}_{P_{ij}} - \hat{\mathbf{y}}_{P_{ij}} \tag{19}$$

substituting from (11a), (17), and (18) into (19) and disregarding higher order terms,

$$\delta\mathbf{y}_{p_{ij}} \approx \delta\mathbf{p}_j^n - \delta\mathbf{p}_i^n + \boldsymbol{\eta}_{p,J_{ij}} + \mathbf{R}_{b_j}^{p_j}\delta\mathbf{l}_{ji}^{b_j} - \mathbf{R}_{b_i}^{p_i}\delta\mathbf{l}_{ij}^{b_i} - \hat{\mathbf{l}}_{ji}^{p_j} \times \boldsymbol{\phi}_j + \hat{\mathbf{l}}_{ij}^{p_i} \times \boldsymbol{\phi}_i \tag{20}$$

where $\delta\mathbf{l}_{ij}^{b_i} \in \mathbb{R}^3$ and $\delta\mathbf{l}_{ji}^{b_j} \in \mathbb{R}^3$ are vectors of segment estimation errors.

Each joint's velocity is obtainable from an adjacent link module,

$$\mathbf{v}_{J_{ij,i}}^n = \mathbf{v}_i^n + \mathbf{R}_{b_i}^n(\boldsymbol{\omega}_{ib_i}^{b_i} \times \mathbf{l}_{ij}^{b_i}) \tag{21}$$

while $\mathbf{v}_{J_{ij,i}}^n$ is the velocity of joint J_{ij} obtained from the parameters of the ith link. Similar to the joint positions, $\mathbf{v}_{J_{ij,i}}^n$ and $\mathbf{v}_{J_{ij,j}}^n$ are not exactly equivalent as a result of joint deformations during motions. To enforce the equivalency constraint between $\mathbf{v}_{J_{ij,i}}^n$ and $\mathbf{v}_{J_{ij,j}}^n$ the next pseudo-measurement vector is defined by considering (21) to model joint deformations,

$$\tilde{\mathbf{y}}_{v_{ij}} = \mathbf{v}_j^n - \mathbf{v}_i^n + \boldsymbol{\eta}_{v,J_{ij}} + \mathbf{R}_{b_j}^n(\boldsymbol{\omega}_{ib_j}^{b_j} \times \mathbf{l}_{ji}^{b_j}) - \mathbf{R}_{b_i}^n(\boldsymbol{\omega}_{ib_i}^{b_i} \times \mathbf{l}_{ij}^{b_i}) \tag{22}$$

where the diagonal covariance matrix of $\boldsymbol{\eta}_{v,J_{ij}} \in \mathbb{R}^3$ is $\sigma_{v,J_{ij}}\mathbf{I}_{3\times3}$ with $\sigma_{v,J_{ij}} > 0$ representing the axiswise noise SD. Considering (22) and (5a),

$$\hat{\mathbf{y}}_{v_{ij}} = \hat{\mathbf{v}}_j^n - \hat{\mathbf{v}}_i^n + \mathbf{R}_{b_j}^{p_j}(\hat{\boldsymbol{\omega}}_{ib_j}^{b_j} \times \hat{\mathbf{l}}_{ji}^{b_j}) - \mathbf{R}_{b_i}^{p_i}(\hat{\boldsymbol{\omega}}_{ib_i}^{b_i} \times \hat{\mathbf{l}}_{ij}^{b_i}) \tag{23}$$

The joint velocity residual vector, $\delta\mathbf{y}_{v_{ij}} \in \mathbb{R}^3$, is defined as,

$$\delta\mathbf{y}_{v_{ij}} = \tilde{\mathbf{y}}_{v_{ij}} - \hat{\mathbf{y}}_{v_{ij}} \tag{24}$$

Substituting (11a), (22), and (23) to (24) and ignoring higher order terms results in,

$$\begin{aligned}\delta\mathbf{y}_{v_{ij}} \approx{}& \delta\mathbf{v}_j^n - \delta\mathbf{v}_i^n + \boldsymbol{\eta}_{v,J_{ij}} - (\mathbf{R}_{b_j}^{p_j}(\hat{\boldsymbol{\omega}}_{ib_j}^{b_j} \times \hat{\mathbf{l}}_{ji}^{b_j})) \times \boldsymbol{\phi}_j + (\mathbf{R}_{b_i}^{p_i}(\hat{\boldsymbol{\omega}}_{ib_i}^{b_i} \times \hat{\mathbf{l}}_{ij}^{b_i})) \times \boldsymbol{\phi}_i \\ &+\mathbf{R}_{b_j}^{p_j}(\delta\boldsymbol{\omega}_{ib_j}^{b_j} \times \hat{\mathbf{l}}_{ji}^{b_j} + \hat{\boldsymbol{\omega}}_{ib_j}^{b_j} \times \delta\mathbf{l}_{ji}^{b_j}) - \mathbf{R}_{b_i}^{p_i}(\delta\boldsymbol{\omega}_{ib_i}^{b_i} \times \hat{\mathbf{l}}_{ij}^{b_i} + \hat{\boldsymbol{\omega}}_{ib_i}^{b_i} \times \delta\mathbf{l}_{ij}^{b_i})\end{aligned} \tag{25}$$

It is noteworthy that $\boldsymbol{\eta}_{p,J_{ij}}$ and $\boldsymbol{\eta}_{v,J_{ij}}$, in (17) and (22), are included to model the joints' deformations.

The measurement and estimation of $\mathbf{p}_c$, the position of the camera (Fig. 1), which can be obtained by the SLAM and the kth module data, should be equivalent. To impose the equivalence constraint between these two, since the SLAM provides the direct position of the camera,

$$\tilde{\mathbf{y}}_{p_c} = \tilde{\mathbf{p}}_c^n = \mathbf{p}_0^n + \mathbf{R}_{b_0}^n \mathbf{l}_c^{b_0} + \boldsymbol{\eta}_{p_c} \tag{26}$$

where $\tilde{\mathbf{p}}_c^n$ is the position obtained from the output of the SLAM and the diagonal covariance matrix of $\boldsymbol{\eta}_{p_c} \in \mathbb{R}^3$ is $\sigma_{p_c}\mathbf{I}_{3\times3}$ with $\sigma_{p_c} > 0$ representing the axiswise noise SD. According to (26) and (5a),

$$\hat{\mathbf{y}}_{p_c} = \hat{\mathbf{p}}_c^n = \hat{\mathbf{p}}_0^n + \mathbf{R}_{b_0}^{p_0}\hat{\mathbf{l}}_c^{b_0} \tag{27}$$

The camera position residual vector, $\delta\mathbf{y}_{p_c} \in \mathbb{R}^3$, is defined as,

$$\delta\mathbf{y}_{p_c} = \tilde{\mathbf{y}}_{p_c} - \hat{\mathbf{y}}_{p_c} \tag{28}$$

substituting from (11a), (26), and (27) into (28) and disregarding higher order terms,

$$\delta\mathbf{y}_{p_c} \approx \delta\mathbf{p}_c^n - \delta\mathbf{p}_0^n - \boldsymbol{\eta}_{p_c} - \mathbf{R}_{b_0}^{p_0}\delta\mathbf{l}_c^{b_0} + \hat{\mathbf{l}}_c^{p_0} \times \boldsymbol{\phi}_0 \tag{29}$$

where $\delta\mathbf{l}_c^{b_0} \in \mathbb{R}^3$ is the camera lever arm estimation error vector. Notably, the SLAM output frequency is disordered, variable, and about one-third of the IMU's frequency. Thus, the algorithm uses measurement (29) each time the SLAM provides data.

The estimated attitude for each module is corrected with the aid of the accelerometer measurements. Ideally, the output norms of static tri-axis accelerometers are close to the gravitational force. When the kth link is steady, the gravity vector is obtainable as,

$$\mathbf{g}^n = -\mathbf{R}_{b_k}^n \mathbf{f}_k^{b_k} \tag{30}$$

Considering (5a), (30), and the estimated gravity vector during stationary periods,

$$\hat{\mathbf{g}}^n = -\mathbf{R}_{b_k}^{p_k}\hat{\mathbf{f}}_k^{b_k} \tag{31}$$

During stationary periods, the gravity vector and its estimate provide a vertical reference. Consequently, the gravity measurement residual, $\delta\mathbf{g}^n \in \mathbb{R}^3$, is defined as,

$$\delta\mathbf{g}^n = \mathbf{g}^n - \hat{\mathbf{g}}^n \tag{32}$$

Substituting (11a), (30), and (31) into (32) results in,

$$\delta\mathbf{g}^n \approx -\mathbf{g}^n \times \boldsymbol{\phi}_k - \delta\mathbf{f}_k^n \tag{33}$$

The augmented state and estimation error vectors are denoted by $\mathbf{x}$ and $\mathbf{e}$, respectively, and defined by,

$$\begin{aligned}\mathbf{x} &= \left[\mathbf{x}_1{}^T \quad \mathbf{x}_2{}^T \quad \cdots \quad \mathbf{x}_N{}^T \quad \left(\mathbf{l}_c^{b_0}\right)^T\right]^T, \\ \mathbf{e} &= \left[\mathbf{e}_1{}^T \quad \mathbf{e}_2{}^T \quad \cdots \quad \mathbf{e}_N{}^T \quad \left(\delta\mathbf{l}_c^{b_0}\right)^T\right]^T\end{aligned} \tag{34}$$

Where $\mathbf{x}_k, \mathbf{e}_k \quad (k = 1, \ldots, N)$ denote the augmented state and estimation error vectors of the kth module and N is the total number of the modules.

$$\begin{aligned}\mathbf{x}_k &= \Big[\left(\mathbf{p}_k^n\right)^T \quad \left(\mathbf{v}_k^n\right)^T \quad \left(\mathbf{q}_{p_k}^n\right)^T \quad \left(\mathbf{b}_{a,k}\right)^T \cdots \\ &\quad \cdots \left(\mathbf{b}_{g,k}\right)^T \quad \left(\mathbf{l}_{k,k+1}^{b_k}\right)^T \quad \left(\mathbf{l}_{k,k-1}^{b_k}\right)^T\Big]^T, \\ \mathbf{e}_k &= \Big[\left(\delta\mathbf{p}_k^n\right)^T \quad \left(\delta\mathbf{v}_k^n\right)^T \quad \left(\boldsymbol{\phi}_k\right)^T \quad \left(\delta\mathbf{b}_{a,k}\right)^T \cdots \\ &\quad \cdots \left(\delta\mathbf{b}_{g,k}\right)^T \quad \left(\delta\mathbf{l}_{k,k+1}^{b_k}\right)^T \quad \left(\delta\mathbf{l}_{k,k-1}^{b_k}\right)^T\Big]^T\end{aligned} \tag{35}$$

Note that $\mathbf{x}_k$ and $\mathbf{e}_k$ respectively use unit quaternions and rotation vectors to parameterize the attitude.

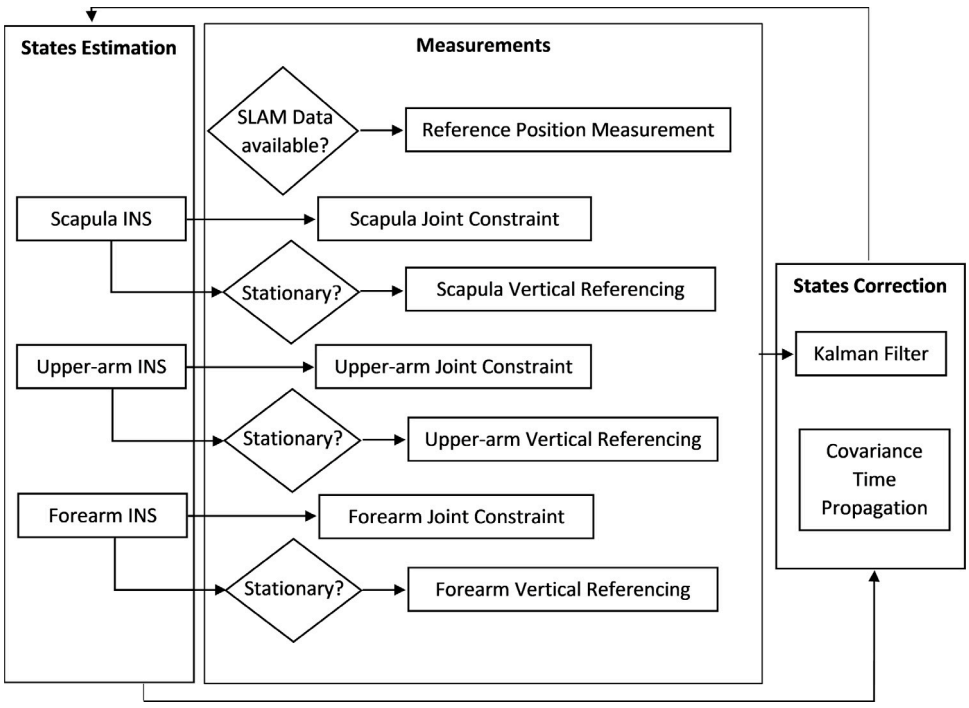

Fig. 2. The overall flowchart of the data fusion algorithms.

Table 2
Kalman filter schemes.

Filter	Propagation	Correction
EKF	(6), (13), (14), and (15)	(20), (25), (29), and (33)
SRUKF	(6)	(19), (24), (28), and (32)

Table 3
Sensor noise characteristics.

Sensor	Random walk	Bias instability
Accelerometer	60 $\mu g/\sqrt{h}$	15 μg
Gyroscope	0.01 $^{\circ}/s/\sqrt{h}$	10 $^{\circ}/h$

An effective method for sensor fusion is the Kalman filter which has two main stages: time propagation of the states and error covariance by system dynamics, followed by states and error covariance correction by measurements. The performance of the Kalman filter in the correction of the parameter estimations obtained by the numerical integration of (6) is evaluated using extended and unscented schemes. The extended Kalman filter uses (13), (14), and (15) for attitude, velocity, and position error dynamics, respectively. The unscented Kalman filter is implemented using square-root covariance propagation and update for increased numerical stability similar to the method introduced in [24]. Due to the large number of the estimated states (i.e. 60 states, including 27 variables and 33 constants in the human arm motion tracking as discussed in Section 5), the SRUKF algorithm is implemented to mitigate the numerical instability issues encountered by the conventional UKF algorithm. The α and β parameters that are responsible for sigma points distribution in the SRUKF algorithm [24] are considered to be 1 and 2, respectively. The related equations for the propagation and correction stages of each Kalman filter are tabulated in Table 2. The overall flowchart of the data fusion algorithms is presented in Fig. 2.

5. Experimental results

In this section, the proposed algorithms' performance in human arm motions is experimentally assessed against a VICON optical motion capture system, which has a measurement error of less than 2 mm [25]. These tests were conducted during 9 fast-paced gait (simple walking) and 3 jumping (walking and occasional jumps) motion scenarios on rectangular-shaped and straight paths (moving forward and backward without turning). The reference frame alignment between the inertial and optical systems is done using the method proposed in [26]. The subject traveled up to 200 m in over 180 s during each test.

The arm is composed of 3 links (including the forearm, upper-arm, and scapula), 2 joints (including the elbow and shoulder), and 4 segments and one camera lever arm (Fig. 1). Thus, the objective of the resulting estimation problem is to determine the position, velocity, and attitude of each 3 links at each point in time (i.e. 27 variables) as well as segment vectors (4 segments between links and joints), sensor biases (3 tri-axis accelerometer and 3 tri-axis gyroscope biases), and camera lever arm (i.e. 33 constants), which results in 60 estimated states.

The system hardware used to evaluate the performance of the algorithms were 3 MTx Xsens modules and a smartphone camera (S21 Ultra ultra-wide camera, 12 MP, F2.2) for the SLAM system (Fig. 1). The IMUs data were recorded in 100 Hz and the visual data was fed to the SLAM system in 60 FPS and 640 × 480 resolution. The frequency of the output of ORB-SLAM3 reference position measurements is in the range of 15–25 Hz. The process noise characteristics in the proposed estimation algorithms are set using the noise characteristics of the sensors presented in Table 3. The initial SDs for estimation errors of position, velocity, attitude, gyroscope bias, accelerometer bias, and segments are assumed to be 10 cm, 1 cm/s, 1 deg, 0.1 deg/s, 0.1 m/s^2, and 10 cm, respectively. The SD values for position and velocity measurement noise responsible for modeling joint deformations in (20) and (25) are set at 1 cm and 1 cm/s, respectively. The above values are established by trial and error. The SD value of the SLAM position measurement noise in (29) is set to 5 cm according to the monocular ORB-SLAM3 RMSE ATE reported in [18].

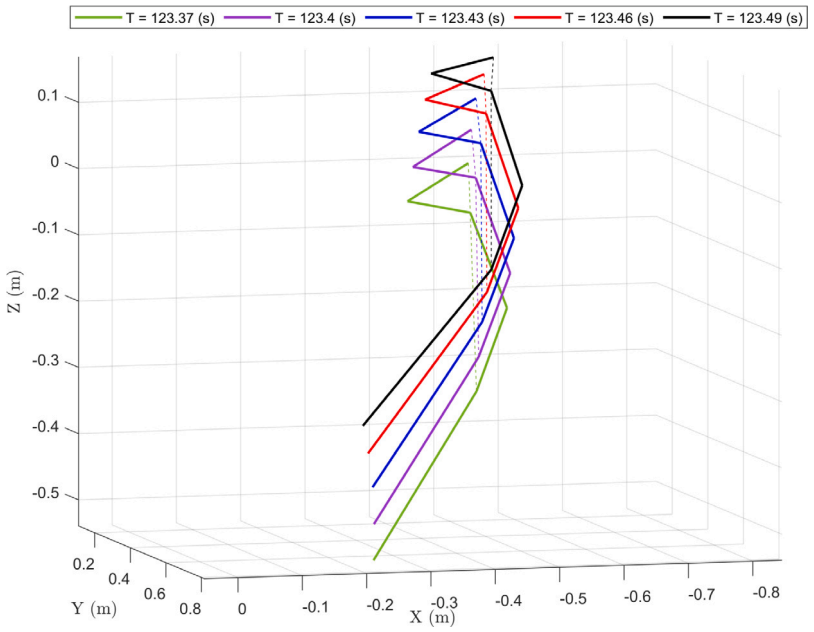

Fig. 3. The estimated poses of the arm in multiple consecutive time frames during a jumping motion scenario using the SRUKF-S scheme.

To assess the effects of shoulder position measurement errors and frequency disorders of the SLAM system on the algorithm performance, both the EKF and SRUKF algorithms were implemented once using SLAM position output obtained from the smartphone camera data, denoted by EKF-S and SRUKF-S, and once using absolute position measurements obtained from VICON, denoted by EKF-V and SRUKF-V. Notably, the VICON measurements used for data fusion algorithms error control are restricted only to the shoulder position. The position and attitude of the other links are estimated through the fusion of IMU measurements integrated over time and the imposing of biomechanical pseudo-measurements. The estimated poses of the arm in multiple consecutive time frames during a jumping motion scenario using the SRUKF-S scheme are illustrated in Fig. 3. The reconstructed trajectory and map point of the executed SLAM (ORB-SLAM3 [18]) as the position measurement for the EKF-S and SRUKF-S algorithms are shown in Fig. 4. ORB-SLAM3 has been implemented in the monocular scheme. In order to obtain more reliable reference position measurement data out of ORB-SLAM3, the camera data were recorded 30 to 45 s ahead of the IMU data so that ORB-SLAM3 calibrated itself with the laboratory environment. The results of the proposed algorithms are shown in Figs. 5–9. The position and attitude estimation root mean square error (RMSE) for each dataset is calculated over its duration. The statistical position and attitude estimation error results for the shoulder, upper-arm, and forearm among 9 gait and 3 jumping scenarios are reported in Table 4. The mean cycle run time for the EKF and SRUKF algorithms are 7.15 (ms) and 17.24 (ms), respectively, meaning that the SRUKF algorithm is about 2.4 times more computationally demanding than the EKF. Notably, the timing results were measured while the proposed algorithms were deployed under MATLAB and were run on a 3.6 GHz quad-core processor.

Table 4
Statistical position and attitude estimation error results.

Algorithm	Joint	Mean position RMSE (cm)	Position RMSE SD (cm)	Mean attitude RMSE (deg)	Attitude RMSE SD (deg)
EKF-S	Scapula	14.03	2.28	4.54	1.1
	Upperarm	12.93	3.21	2.94	1.48
	Forearm	17.34	2.85	6.1	1.77
SRUKF-S	Scapula	14.98	3.97	4.11	1.11
	Upperarm	14.65	3.62	2.2	1.4
	Forearm	21.38	6.67	6.17	2.22
EKF-V	Scapula	10.87	1.52	4.08	1.12
	Upperarm	7.1	1.76	2.07	0.91
	Forearm	15.64	2.53	5.76	1.94
SRUKF-V	Scapula	10.15	1.47	3.9	1.09
	Upperarm	9.12	1.8	2.23	1.52
	Forearm	17.89	5.26	6.18	2.16

6. Discussion

The estimated planar trajectory of the shoulder in a rectangular-shaped path gait test in comparison with the VICON is presented in Fig. 5. As expected, the EKF-V and SRUKF-V trajectories are closer to the VICON ground-truth compared to the EKF-S and SRUKF-S due to their more accurate reference position measurements. The forearm link position and attitude estimations and their estimations errors compared to the VICON are illustrated in Figs. 6, 7 because it is the most challenging link due to its faster movements and distance from the camera. All the figures present position in the n-frame and attitude in terms of Euler angles. As shown in Fig. 7, the SLAM output error and frequency disorders caused more errors in EKF-S and SRUKF-S compared to EKF-V and SRUKF-V.

Gyroscope biases, accelerometer biases, and segment estimations in Figs. 8, 9 show smoother convergence and higher convergence rates for SRUKF algorithms versus EKF algorithms. Moreover, according to Fig. 8, the SRUKF estimation of the biases fluctuates less than the EKF, especially in the case of accelerometer bias. Furthermore, the SRUKF estimation of sensor biases and segments is not only faster in convergence, but also more stable. There is hardly any difference in the convergence rate of the sensor biases estimation between the SLAM and VICON position measurements (Fig. 8). Assuming that no prior knowledge of the body geometry is available, initial estimations for segment lengths are set at zero. The convergence of the scapula to the camera segment length differs significantly between SLAM and VICON position measurements due to the SLAM output errors (Fig. 9). This difference decreases as the distance between the segment and the camera increases. The difference between the segment length convergence in SLAM and VICON position measurements from the shoulder joint downwards is insignificant (Fig. 9). This decrease is explicable because

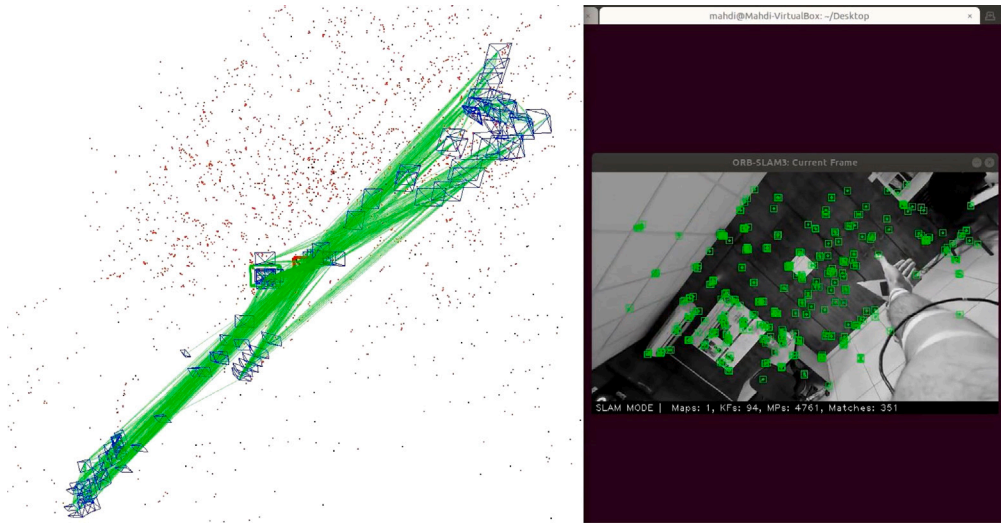

Fig. 4. ORB-SLAM3 reconstructed trajectory and map point.

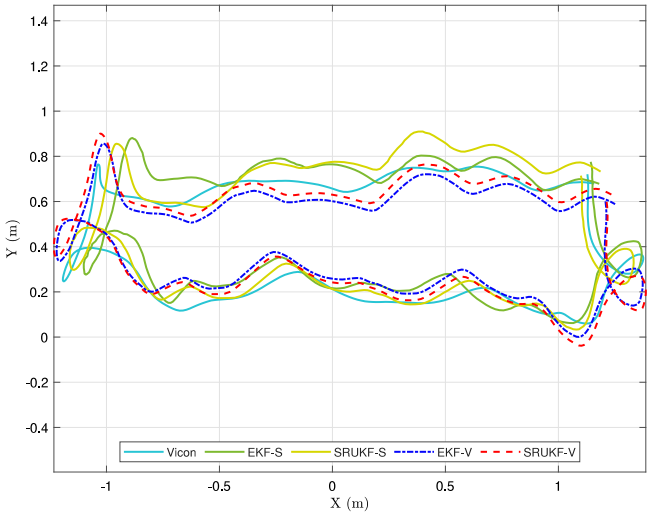

Fig. 5. Scapula link planar trajectory during a jumping scenario.

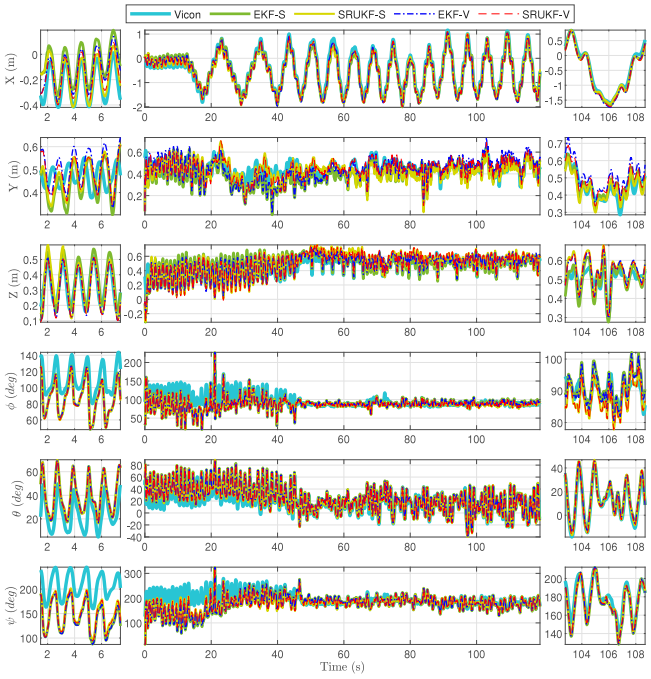

Fig. 6. Forearm link position and attitude estimation compared to the VICON during a jumping scenario.

the biomechanical constraint measurements attenuate the effects of SLAM position measurement noise and errors.

As reported in Table 4, the minimum position and attitude estimation RMSEs across all links for the EKF-S, SRUKF-S, EKF-V, and SRUKF-V are 6.66 (cm) and 1.1 (deg), 5.87 (cm) and 1.11 (deg), 3.39 (cm) and 0.91 (deg), and 6.28 (cm) and 1.09 (deg), respectively. EKF-S is up to 80% and 40% less accurate than EKF-V, and SRUKF-S is up to 60% and 6% less accurate than SRUKF-V, in position and attitude estimation, respectively. These results were expected because of the lower estimation error and higher data frequency of the VICON reference position measurement compared to the SLAM output. It is evident that the SRUKF-S algorithm is more resistant to SLAM errors and disordered frequencies than the EKF-S.

As shown in Figs. 8, 9, the convergence rate of the sensor biases and segments is faster and smoother for the SRUKF algorithms, which represents the main advantage of SRUKF algorithms in exchange for a higher computational cost. Table 4 results show that the SRUKF-S is up to 17% less and 36% more accurate than the EKF-S in position and attitude estimation, respectively. In the case of EKF-V and SRUKF-V algorithms, the difference varies from link to link. In the scapula link, SRUKF-V is 8% and 6% more accurate than EKF-V, in position and attitude estimation, respectively. But in the upper-arm, link SRUKF-V is 12% and 6% less accurate than EKF-V, in position and attitude estimation, respectively.

7. Conclusion

Inertial motion capture algorithms using extended and square-root unscented Kalman filtering in combination with the SLAM method are proposed. The algorithms estimate the sensor biases and link geometries in addition to the positions, velocities, and attitudes. The

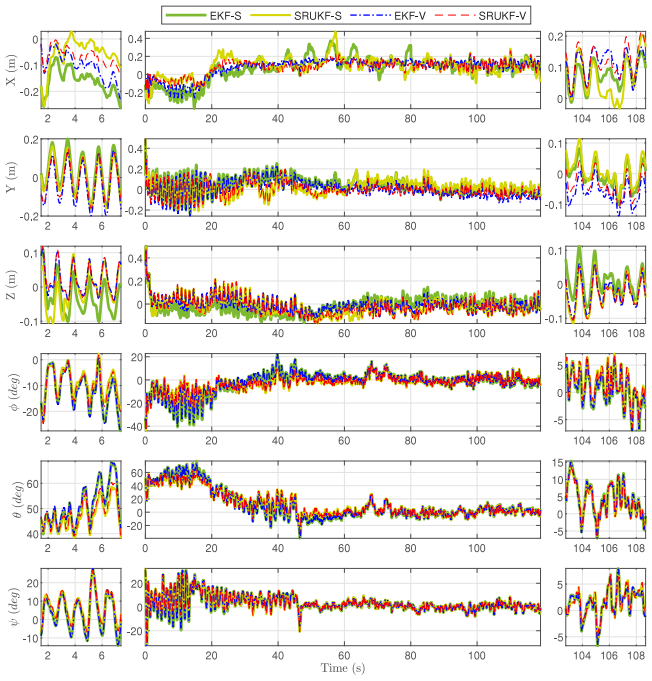

Fig. 7. Error of forearm link position and attitude estimation compared to VICON optical motion capture system during a jumping scenario.

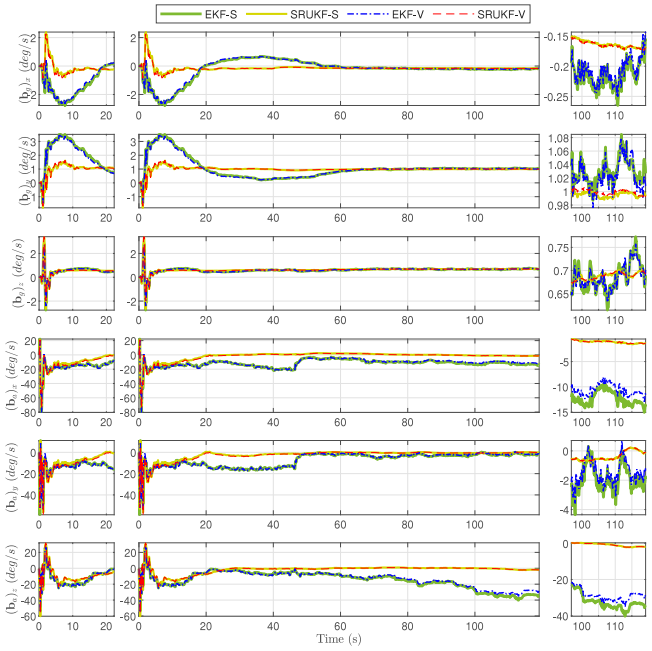

Fig. 8. Gyroscope and accelerometer bias estimation during a jumping scenario.

capability of the algorithm in estimating the link geometries and segments allows the imposition of biomechanical constraints without *a priori* knowledge of the sensors and the camera's positions. Without relying on magnetic measurements and taking advantage of SLAM position output, the system is applicable in outdoor, non-laboratory, and unknown environments. The performance of the proposed algorithms was evaluated compared to the VICON optical motion capture system during 9 fast-paced gait and 3 jumping motion scenarios.

To study the effects of measurement errors and frequency variations on estimation performance, the algorithms were implemented once

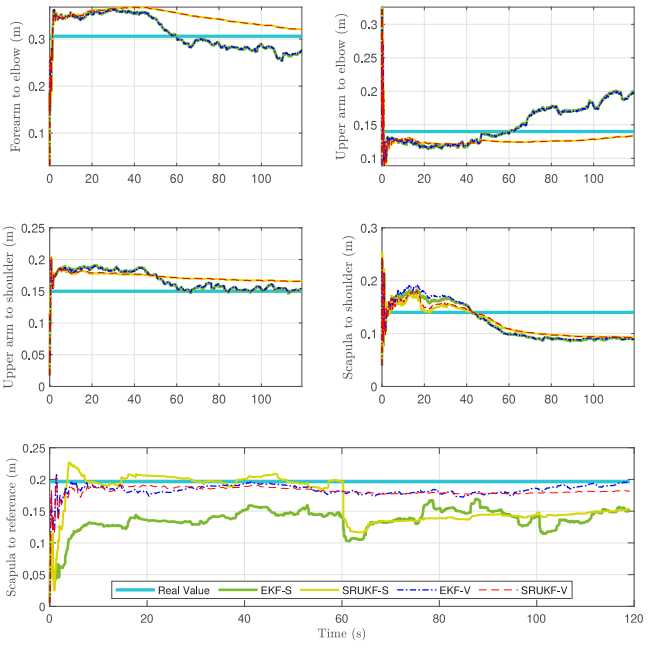

Fig. 9. Segments length estimation during a jumping scenario.

using the SLAM outputs and once using VICON as position measurements. Expectedly, the VICON's absolute position measurements yield less position and attitude estimation errors than SLAM, specifically in the EKF algorithms. The SRUKF algorithms present a remarkably smoother and higher convergence rate compared to the EKF. The SRUKF and EKF algorithms' estimation errors after convergence are very similar and vary from link to link. In addition, the SRUKF algorithms are 2.4 times more time-consuming than the EKF algorithms. This difference in computational cost increases as the number of the estimated states increases as well.

Future research may suggest a new approach for Kalman filtering by using hybrid filters to reduce the computational cost of the SRUKF algorithm while taking advantage of its high convergence rate. Moreover, the feasibility of position and attitude estimation of the whole body with an IMU placed on each link and one or two cameras placed on the shoulder, chest, or back of the subject via proposed algorithms can be studied in future works.

CRediT authorship contribution statement

Mohammad Mahdi Azarbeik: Conceptualization, Methodology, Software, Validation, Formal analysis, Investigation, Writing – original draft, Visualization. **Hamidreza Razavi:** Conceptualization, Methodology, Investigation, Resources, Writing – original draft. **Kaveh Merat:** Methodology, Resources. **Hassan Salarieh:** Resources, Supervision.

Declaration of competing interest

The authors declare that they have no known competing financial interests or personal relationships that could have appeared to influence the work reported in this paper.

Data availability

The data of this research is available on the IEEE data port. (https://ieee-dataport.org/documents/human-arm-motion-tracking-fusion-imu-modules-and-slam-method-compared-vicon).

Acknowledgments

This submitted paper has been uploaded on the arXiv pre-print server. (https://arxiv.org/abs/2302.08294v1)

Funding

The authors declare that no funds, grants, or other support were received during the preparation of this manuscript.

Appendix A. Supplementary data

Supplementary material related to this article can be found online at https://doi.org/10.1016/j.measurement.2023.113690.

References

[1] T. McGrath, L. Stirling, Body-worn IMU human skeletal pose estimation using a factor graph-based optimization framework, Sensors (ISSN: 1424-8220) 20 (23) (2020) 6887.
[2] S.-h. Lee, D.-W. Lee, K. Jun, W. Lee, M.S. Kim, Markerless 3D skeleton tracking algorithm by merging multiple inaccurate skeleton data from multiple RGB-d sensors, Sensors (ISSN: 1424-8220) 22 (9) (2022) 3155.
[3] M. Naeemabadi, B. Dinesen, O.K.s. Andersen, J. Hansen, Influence of a marker-based motion capture system on the performance of microsoft kinect v2 skeleton algorithm, IEEE Sens. J. (ISSN: 1530-437X) 19 (1) (2018) 171–179.
[4] A. Pfister, A.M. West, S. Bronner, J.A. Noah, Comparative abilities of microsoft kinect and vicon 3D motion capture for gait analysis, J. Med. Eng. Technol. (ISSN: 0309-1902) 38 (5) (2014) 274–280.
[5] S. Asteriadis, A. Chatzitofis, D. Zarpalas, D.S. Alexiadis, P. Daras, Estimating human motion from multiple kinect sensors, in: Proceedings of the 6th International Conference on Computer Vision/Computer Graphics Collaboration Techniques and Applications, 2013, pp. 1–6.
[6] V. Bijalwan, V.B. Semwal, T. Mandal, Fusion of multi-sensor-based biomechanical gait analysis using vision and wearable sensor, IEEE Sens. J. (ISSN: 1530-437X) 21 (13) (2021) 14213–14220.
[7] A. Ahmadi, F. Destelle, D. Monaghan, K. Moran, N.E. O'Connor, L. Unzueta, M.T. Linaza, Human gait monitoring using body-worn inertial sensors and kinematic modelling, in: 2015 IEEE SENSORS, IEEE, 2015, pp. 1–4.
[8] T. Kaichi, T. Maruyama, M. Tada, H. Saito, Learning sensor interdependencies for IMU-to-segment assignment, IEEE Access (ISSN: 2169-3536) 9 (2021) 116440–116452.
[9] I. Kecskés, A. Odry, V. Tadić, P. Odry, Simultaneous calibration of a hexapod robot and an imu sensor model based on raw measurements, IEEE Sens. J. 21 (13) (2021) 14887–14898.
[10] I. Weygers, M. Kok, H. De Vroey, T. Verbeerst, M. Versteyhe, H. Hallez, K. Claeys, Drift-free inertial sensor-based joint kinematics for long-term arbitrary movements, IEEE Sens. J. (ISSN: 1530-437X) 20 (14) (2020) 7969–7979.
[11] M. Dong, G. Yao, J. Li, L. Zhang, Calibration of low cost imu's inertial sensors for improved attitude estimation, J. Intell. Robot. Syst. 100 (2020) 1015–1029.
[12] J. Wu, Z. Zhou, J. Chen, H. Fourati, R. Li, Fast complementary filter for attitude estimation using low-cost marg sensors, IEEE Sens. J. (ISSN: 1530-437X) 16 (18) (2016) 6997–7007.
[13] Z. Wu, Z. Sun, W. Zhang, Q. Chen, A novel approach for attitude estimation based on MEMS inertial sensors using nonlinear complementary filters, IEEE Sens. J. (ISSN: 1530-437X) 16 (10) (2016) 3856–3864.
[14] E. Francelino, M. Pereira, R. Inoue, M. Terra, A. Siqueira, S. Nogueira, Markov system with self-aligning joint constraint to estimate attitude and joint angles between two consecutive segments, J. Intell. Robot. Syst. 104 (3) (2022) 43.
[15] A. Atrsaei, H. Salarieh, A. Alasty, Human arm motion tracking by orientation-based fusion of inertial sensors and kinect using unscented Kalman filter, J. Biomech. Eng. (ISSN: 0148-0731) 138 (9) (2016).
[16] A. Atrsaei, H. Salarieh, A. Alasty, M. Abediny, Human arm motion tracking by inertial/magnetic sensors using unscented Kalman filter and relative motion constraint, J. Intell. Robot. Syst. (ISSN: 1573-0409) 90 (1) (2018) 161–170.
[17] H. Razavi, H. Salarieh, A. Alasty, Towards real-time partially self-calibrating pedestrian navigation with an inertial sensor array, IEEE Sens. J. (ISSN: 1530-437X) 20 (12) (2020) 6634–6641.
[18] C. Campos, R. Elvira, J.J.G. Rodríguez, J.M. Montiel, J.D. Tardós, Orb-slam3: An accurate open-source library for visual, visual–inertial, and multimap slam, IEEE Trans. Robot. (ISSN: 1552-3098) 37 (6) (2021) 1874–1890.
[19] C. Forster, Z. Zhang, M. Gassner, M. Werlberger, D. Scaramuzza, SVO: Semidirect visual odometry for monocular and multicamera systems, IEEE Trans. Robot. (ISSN: 1552-3098) 33 (2) (2016) 249–265.
[20] G. Li, L. Yu, S. Fei, A binocular MSCKF-based visual inertial odometry system using lk optical flow, J. Intell. Robot. Syst. 100 (2020) 1179–1194.
[21] L. Wang, Y. Sun, Q. Li, T. Liu, Estimation of step length and gait asymmetry using wearable inertial sensors, IEEE Sens. J. (ISSN: 1530-437X) 18 (9) (2018) 3844–3851.
[22] E.-H. Shin, Estimation techniques for low-cost inertial navigation, UCGE Rep. 20219 (2005).
[23] K.J. Åström, Introduction To Stochastic Control Theory, Courier Corporation, Massachusetts, 2012.
[24] R. Van Der Merwe, E.A. Wan, The square-root unscented Kalman filter for state and parameter-estimation, in: 2001 IEEE International Conference on Acoustics, Speech, and Signal Processing. Proceedings (Cat. No. 01CH37221), vol. 6, IEEE, ISBN: 0780370414, pp. 3461–3464.
[25] P. Merriaux, Y. Dupuis, R. Boutteau, P. Vasseur, X. Savatier, A study of vicon system positioning performance, Sensors (ISSN: 1424-8220) 17 (7) (2017) 1591.
[26] H. Razavi, H. Salarieh, A. Alasty, Inertial motion capture accuracy improvement by kalman smoothing and dynamic networks, IEEE Sens. J. (ISSN: 1530-437X) 21 (3) (2020) 3722–3729.